symmetry

MDPI

Article

Analysis of Traction and Unfolding Dynamics of Space-Symmetric Flexible Webs for UAV Interception and Capture

Yiming Liu, Ziming Xiong *, Yanyu Qiu, Fuhuai Yan and Chao Ma

State Key Laboratory of Disaster Prevention & Mitigation of Explosion & Impact, Army Engineering University of PLA, Nanjing 210007, China
* Correspondence: xzm992311@163.com

Abstract: A new type of flexible web with a spatial symmetry structure is proposed to address the interception and acquisition of UAVs. It is different from the existing flexible web structure. According to the mechanical characteristics of the flexible web, the dynamic analysis model of the flexible web is established through theoretical deduction. Through finite element simulation calculation, the flexible webs of three different spatial symmetric structures are compared and analyzed. The internal force and air attitude of the three flexible webs are discussed. Among them, the new flexible web has a lag time of 0.162 s and a flight height of 11.624 m. The above simulation parameters are better than those of the other two symmetrical structures. It was proved that the new spatial symmetric flexible web has good traction and deployment performance. In addition, a ground verification test is designed and carried out. The web attitude and flight altitude parameters are compared with the simulation and test results. It is found that the simulation and experimental process of the new symmetric structure web are in good agreement, the synchronization of attitude change is good, and the flight altitude error of the two is controlled at about 5%. The feasibility and effectiveness of this method are proven and it can provide a reference for the research of flexible interception and acquisition of UAVs.

Keywords: space flexible web; traction unfolding dynamics; expand dynamic theoretical model; simulation analysis; ground test

Citation: Liu, Y.; Xiong, Z.; Qiu, Y.; Yan, F.; Ma, C. Analysis of Traction and Unfolding Dynamics of Space-Symmetric Flexible Webs for UAV Interception and Capture. *Symmetry* **2022**, *14*, 1915. https://doi.org/10.3390/sym14091915

Academic Editor: Mihai Postolache

Received: 22 August 2022
Accepted: 6 September 2022
Published: 13 September 2022

1. Introduction

With the continuous development of information technology and intelligent algorithms [1], combat unmanned aerial vehicles (UAVs) are widely used in local wars and high-tech conflicts due to their flexibility, strong concealment and high damage efficiency under the conditions of modern warfare. Current counter-weapons for combat drones include Air Defense Artillery [2], multiple rocket launchers [3], and surface-to-air missiles [4]. In the face of the increasing trend of informatization, integration, and intelligence of drones, the "point-to-point interception" of the counter-weapon mentioned above is gradually insufficient, and the cost-effectiveness ratio is relatively low. As an active interceptor of the new flexible structure, the new space flexible web is pulled out of the storage device by launching a tractor. Then, the new space flexible web spreads out quickly in the air, and in the full arc of the ascent, the target distance sensor controls the EFP (short for Explosively Formed Projectile) high-energy warhead [5] mounted on the new space flexible web to detonate and then attack the incoming UAV, which can effectively compensate for the shortcoming of the traditional anti-aircraft weapon to intercept small windows of space and time by acting as a "gatekeeper" in the form of close-range intercept.

For the interception and capture of UAVs and other targets [6–10], flexible webs with spatially symmetric structures were widely used. Inspired by spider predation, Xu Boting et al. [11] designed a new type of bionic space debris removal device. Moreover, the spin unfolding and collision dynamic models of the flexible web are established, and

the dynamic characteristics of the flexible web unfolding process are simulated by the finite element method. The simulation results effectively reflect the motion characteristics of large deformation and large displacement in capturing the target. In order to solve the "black flying" problem of UAVs, Chen Qingquan et al. [12] proposed a counter-UAV rope web capture method based on flexible rope web aerial deployment capture. On this basis, the dynamic analysis model of the whole process of capture is established, and the platform flight trajectory model and the rope web deployment model are compared with the test results. The feasibility of the dynamic model and simulation idea is verified. Zhou Z.W. et al. [13] developed and designed an anti-UAV web system with low overload launch according to high- and low-pressure launch principles. Through the optimization and analysis of the capture performance and security parameters of the launch system, the overall performance of the anti-UAV web trapping system is improved, which provides theoretical guidance for the countermeasures and capture of the "black fly" UAV. In the study of target acquisition by flexible interception web, the target acquisition process can be divided into four processes: opening, collision, closing and completion. In the whole process of capture, Liu Haitao [14] focused on analyzing the opening dynamic characteristics and parameter optimization of two kinds of flexible rope webs without rotation and with rotation, aiming at the capture and de-orbit problems of the flexible rope web system, and simultaneously studied the rigid–flexible coupling dynamics and de-orbit problems of the rope web and the target assembly after capture.

Due to the advantages of large area coverage, being fast forming, having lightweight flexibility, and low costs, the application of the new space flexible web was extended from the initial capture of non-cooperative objects in space to applications such as slope protection webs [15] and parachutes [16]. The design concept and research methods of the new space flexible web were also used in the research.

At present, most of the research work on space flexible webs is on the structure of rope webs. Under near-ground conditions, the aerodynamic environment is complex, and the spatial preservation of the tethered web is difficult to meet the requirements of combat UAVs. At the same time, unlike small drones, combat drones are larger in mass and volume, have a wider radius of operations, and are more destructive. It is difficult to effectively intercept and destroy combat UAVs by winding capture of the flexible web alone.

The EFP (short for Explosively Formed Projectile) warhead can form a high-speed jet of more than 200 m/s after detonation and can effectively strike the fuel and warhead sections of the incoming target, thus completing the interception of the target. However, the striking effect of the EFP warhead is limited by the high blast range, and the firing direction is not easy to adjust, so based on the current situation of the space flexible web research and the related characteristics of the EFP warhead, a new space flexible web is proposed for the close-range interception of combat UAVs. Through the combination of a flexible intercept web and an EFP combat department, a better intercept effect can be achieved.

This paper establishes a dynamic analysis model of a new type of space flexible web. On this basis, through three different space symmetrical structures, the dynamic simulation of the flexible web, contrast analysis of the parameters such as air posture, movement speed and displacement, combined with the ground test of the new space symmetric structure of the flexible web, proved that the good capability of the sky can provide a reference for the unmanned aerial vehicle (UAV) intercept capture.

2. Brief Introduction of the New Symmetrical Structure Interceptor Web Technology

The new symmetric structure flexible network interception technology system mainly comprises radar detection and tracking, interception control, follow-up emission and a flexible interception network. When the system is switched on, the radar detection part sends out electromagnetic signals and receives echoes from the targets encountered in its detection coverage. The location and other relevant information of the UAV are extracted from the echo signals to detect and track the UAV and realize the purpose of detection, positioning, tracking and recognition. After the threat target is detected, the detection

information is sent to the control solution section at the appropriate time. The control part is connected with the radar detection and follow-up emission parts. It needs to communicate with the detection radar in real-time, receive UAV information, determine UAV trajectory, determine intercept coordinates and optimize launch parameters. The interception process is shown in Figure 1 below.

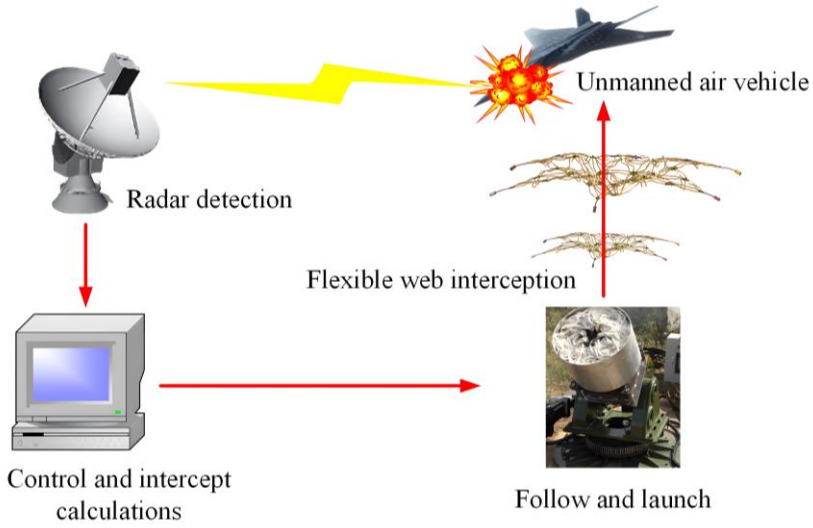

Figure 1. Spatially symmetric structure flexible web intercepting UAV process.

When the UAV enters the interception airspace, the control solution part controls the operation of the follow-up launch part according to the coordinate information of the future interception point, determines the launch azimuth by rotating in both horizontal and pitch directions, launches the new spatial symmetric structure network, and intercepts the incoming UAV.

The new symmetrical flexible net is a countermeasure to intercept UAVs in ultra-short range airspace. By launching an interception net into the air to form the "point-facing" UAV interception airspace, under the appropriate net posture, several EFP warheads loaded on the flexible net detonate to form a high-speed kinetic energy penetration body, intercept and damage the incoming UAV, and then protect our target.

3. Structure and Dynamic Models of Three Space Flexible Webs

As shown in Figure 2 below, the new space flexible web consists mainly of Kevlar fabric strips, Canopies (green), EFP warheads (red), and the centrally located explosion range sensor (blue). Because of the error of transmission synchronization and the influence of crosswinds on the ground, the hexagonal double-stripe topology is designed to make the new space flexible web fuller in the air and more favorable to interception. The main body of the new space flexible web is knitted with high-strength and high-resilience Kevlar fabric strips and node canopies. At the same time, 31 canopies are arranged radially according to a particular geometric relation on the new space flexible web, and the distance sensor is placed on the new space flexible web central canopies. Canopies numbered 13–30 secure one EFP warhead each. Canopies numbered 1–12 reinforce the outer nodes. The primary role of the canopies inside the mesh is to secure the corresponding components and maintain the poise stability of the new spatial flexible mesh and EFP warhead in flight. In Figure 2 below, the numbers in different colors represent the distribution of canopies in different positions.

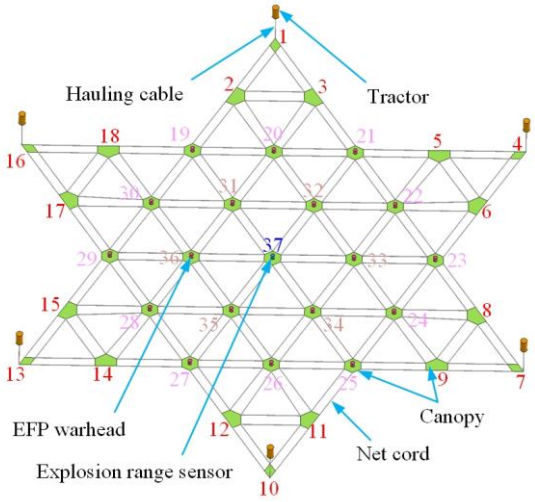

Figure 2. Schematic diagram of a new space flexible web.

In the background of information warfare, combat drones play an essential role in surveillance, fire suppression, and attack missions and are gradually becoming a key force influencing the war's outcome. When a combat UAV strikes, the new type of space flexible web launcher receives the interception signal transmitted by the detection and resolution system. It adjusts the launch pitch and external angle quickly. After ignition and launch, the new space flexible web is pulled from the storage device by six tractors and is rapidly expanded and formed in the air. According to the target characteristics and threat degree of incoming UAVs, the new space flexible web can reach 80% of the maximum area under the temporal and spatial windows between 20 m and 200 m by controlling the amount of propellant and related launch parameters. It is generally believed that the rising concave web posture is fuller under the temporal and spatial windows. When the range sensor is within 100 m of the intercepting target, the EFP combat section fixed on the control detonating parachute will form multiple directed high-energy jets in the air to intercept the combat UAVs in coordination with each other, thus guaranteeing the safety of our high-value economic targets.

In order to further explore the dynamic behavior of the new space flexible web, finite element simulation is introduced to analyze the process of the traditional rope web and a new type of space flexible web. Based on the above two types of webs, the same topological rope web (referred to as the topological rope web) is added to the new type of web. As a transition comparison web, three types of simulation webs are compared: traditional rope web, topological rope web, and a new space flexible web, as shown in Figure 3 below.

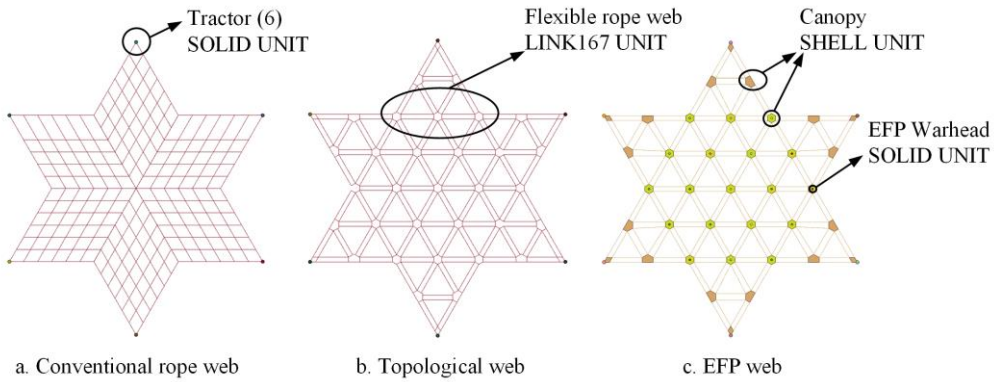

Figure 3. Structure diagram of flexible traditional rope webbing.

This paper analyzes the dynamic characteristics of the three kinds of flexible webs in the course of launchings, such as the tension change of the rope web, the movement parameter changes of the traction body, the deformation of the rope web, and the motion state of the rope segment element. It discusses the dynamic characteristics of the vertical launch of three kinds of flexible webs. It provides a reference for the next step in analyzing launch parameters and ground verification experiments of the new space flexible web.

4. Theoretical Model of the Space Flexible Web Expansion Dynamics

Compared with the space environment, the aerodynamic environment is more complicated under near-ground conditions. In the analysis of the traction and unfolding process of a new space flexible web, considering the particularity of the flexible structure, it is complicated to establish the dynamic formula of the flexible web by considering the rigid and flexible coupling between the flexible web rope and the objects such as the traction body, umbrella and EFP warhead. Based on the above considerations, the geometrical nonlinear response characteristics of the flexible rope system are first introduced by a simple example. Then, two kinds of flexible web structures, traditional rope web, and new spatial flexible web, are rationally simplified. The approximate theoretical model derived after simplification is used to characterize the deployment process of three kinds of flexible webs, and the dynamic model of rope web analysis is established. The launch deployment test of flexible webs in the subsequent research content will verify the rationality and reliability of the dynamic analysis model.

4.1. Geometric Nonlinear Characteristics of the Flexible Web

Because of the particular "tensile and unpressurized" mechanical characteristics of the flexible web, the mechanical response of the wire rope is geometrically nonlinear even if the deformation is small under linear elasticity. In the simple flexible rope system shown in Figure 4 below, the two sides of the rope are fixed at points A and B, the distance between them is L, the stiffness of the flexible rope is EA, and the length of the rope is L_0, the initial strain is ε_0, the initial internal tension is σ_0, and the vertical displacement of the rope is l at the midpoint (M-point) under the action of external force F_0, and the degree of elongation of the rope is ΔL. At this point, the strain increases to ε, the stress increases to σ, and the M-point moves to M_1.

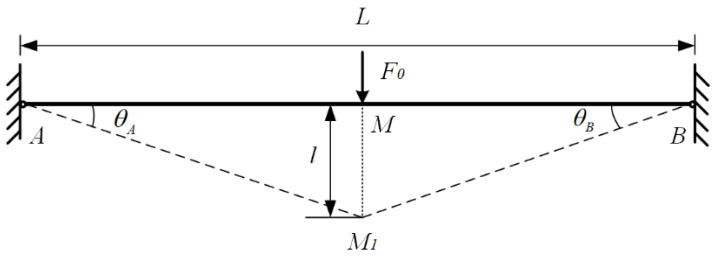

Figure 4. Simple flexible rope system diagram.

As shown in diagram 3, under the action of external force F_0, the rope strain ε is solved as follows:

$$\begin{aligned} \varepsilon = \frac{\Delta L}{L_0} &= \frac{2\left[\frac{\frac{1}{2}L_0\times(1+\varepsilon_0)}{\cos\theta_A} - \frac{1}{2}L_0\right]}{L_0} \\ &= \frac{L_0(1+\varepsilon_0)\sec\theta_A - L_0}{L_0} \\ &= (1+\varepsilon_0)\sec\theta_A - 1 \\ &= (1+\varepsilon_0)\sqrt{\frac{4l^2}{L^2}+1} - 1 \end{aligned} \tag{1}$$

Under the assumption of small elastic deformation on linear elasticity, the following relationships can be used to approximate:

$$\sin\theta_A \approx \frac{l}{\frac{1}{2}L} = \frac{2l}{L} \tag{2}$$

$$\begin{aligned} \varepsilon &= (1+\varepsilon_0)\sqrt{\tfrac{(2l)^2}{L^2}+1}-1 \\ \lim_{\frac{2l}{L}\to 0} &= (1+\varepsilon_0)\left(\tfrac{2l^2}{L^2}+1\right)-1 \end{aligned} \tag{3}$$

From the static equilibrium conditions at the midpoint M_1 of the rope:

$$F_0 = 2\sigma\sin\theta_A \tag{4}$$

The constitutive model of the simple rope system shown in Figure 3 is available under the linear elasticity hypothesis:

$$\sigma = EA\varepsilon\ \varepsilon_0 = \frac{\sigma_0}{EA} \tag{5}$$

The force control equations of simple flexible rope systems (6) can be obtained by combining Formulas (3)–(5):

$$F_0 = (EA+\sigma_0)\frac{8}{L^3}l^3 + \frac{4\sigma_0}{L}l \tag{6}$$

As can be seen from Formula (6), even under the assumption of linear elasticity with small deformation, there is no linear relationship between the external force and displacement of a simple flexible rope. Refer to the flexible rope system in Figure 3, assuming EA = 100,000 N for the stiffness of the rope and L_0 = 2.5 m for the original length of the rope, the relationship between external force and vertical displacement at the midpoint of the web rope is shown in Figure 5 below when the initial internal tension of the rope is 0 N, 200 N, 400 N, 600 N, 800 N, and 1000 N, respectively.

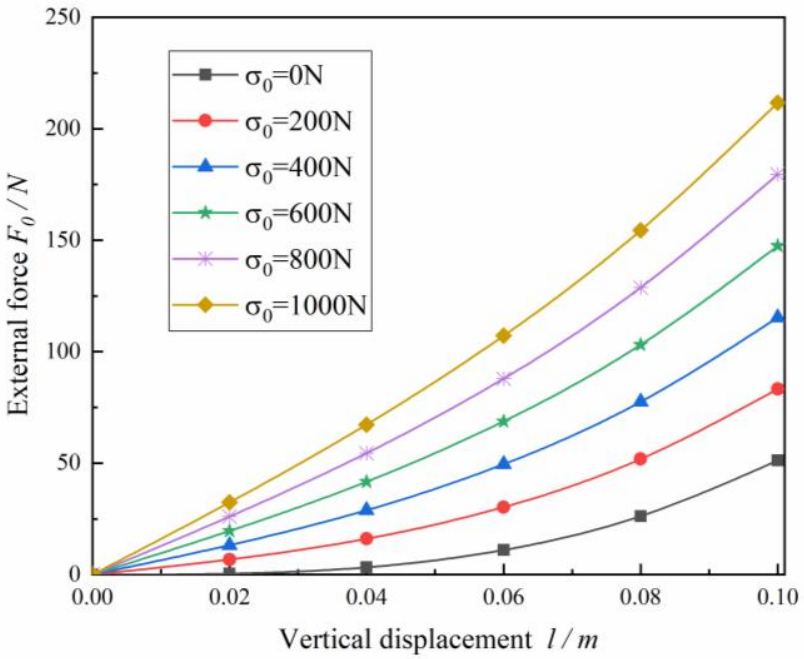

Figure 5. Relationship between external force of flexible rope and vertical displacement of midpoint of rope.

Analyzing Figure 4 above, when the initial internal tension σ_0 of the rope segment is larger, the curve changes faster, and the slope is more extensive, which means the flexible rope is better able to resist external forces. The above examples show that the dynamic problem of webbing rope is different from that of linear system analysis and has prominent nonlinear dynamic characteristics, especially the flexible webbing system in the following chapter.

4.2. Theoretical Model of Traction Expansion Dynamics of Space Flexible Web

4.2.1. Model Assumptions

According to the traditional rope web launch process, the following basic assumptions are made when establishing the rope web launch dynamics model:

(1) Ignore contact effects between flexible web rope segments;
(2) Ignore the shear force and transverse bending moment of the flexible web rope segment;
(3) Ignore the friction effect of flexible web folding storage mode on launch expansion;
(4) The traction body is simplified to a particle in the traction flexible web process;
(5) Ignore the effect of gravity on the emission of the flexible web.

4.2.2. Theoretical Model of Traction Expansion Dynamics

Compared with rigid systems, a new space flexible web is a typical multi-body system with significant motion and large deformation coupling. Establishing an accurate mathematical analysis equation is complex, and its relatively reasonable dynamic analysis model can be built according to the following discrete ideas. Disperse the web rope into finite segments and then the mass of each new spatial flexible strip element is concentrated at the two endpoints, that is, the nodes of each rope segment. Because the cable is very soft, it can only bear the tension along the cable direction and cannot withstand the pressure. Therefore, it can be assumed that the new type of flexible cable node is connected by a virtual "spring," which has the force characteristics of being pulled without pressure. Based on considering the damping effect of the new type of space flexible web, the new type of space flexible mesh segment unit can be treated as a "concentrated mass damping spring model" [17], as shown in Figure 6a below:

In the dynamic model shown in Figure 5 above, the nth new space flexible web segment element is equivalent to a spring damping element whose mass is concentrated at the endpoint, where $m \leq 90$ (a total of 90 rope segment elements), and node n connects node n and node $(m + 1)$ new flexible space bar segment units. Assuming the spring stiffness K_m and damping coefficient ζ_m in the spring damping element, the coordinate components of the node of the nth new space flexible web rope segment are x_m, y_m, z_m, as shown in Figure 6b above.

Figure 7 below shows that the conjoined coordinate system of the nth space flexible web rope segment is $Ox_my_mz_m$, and the x-, y-, and z-axis of the coordinate system corresponds to the primary, secondary, and tangent vectors of the rope curve, respectively. The inertial coordinate system $Ox_ay_az_a$ and the conjoined coordinate system can be determined by three Euler angles: α_m, β_m, and χ_m. The inertial coordinate system can be rotated three times to match the conjoined coordinate system. First, go around the axis Oz_a to the angle β_m, from $Ox_ay_az_a$ to OMy_1z_a; then, turn the α_m corner around ON and go from OMy_1z_a to OMy_2z_m. Finally, round the Oz_m axis to the χ_m angle, from OMy_2z_m to $Ox_my_mz_m$. The transformation matrix of the connective coordinate $Ox_my_mz_m$ and inertial coordinate system $Ox_ay_az_a$ of the space flexible web rope segment is shown in the following Formula (7):

$$B_n = \begin{bmatrix} \cos\chi_m\cos\beta_m - \sin\beta_m\sin\chi_m\cos\alpha_m & \sin\beta_m\cos\chi_m + \sin\chi_m\cos\beta_m\cos\alpha_m & \sin\alpha_m\sin\chi_m \\ -\cos\beta_m\sin\chi_m - \sin\beta_m\cos\alpha_m\cos\chi_m & -\sin\beta_m\sin\chi_m + \cos\alpha_m\cos\beta_m\cos\chi_m & \sin\alpha_m\cos\chi_m \\ \sin\alpha_m\sin\beta_m & -\sin\alpha_m\cos\beta_m & \cos\alpha_m \end{bmatrix} \quad (7)$$

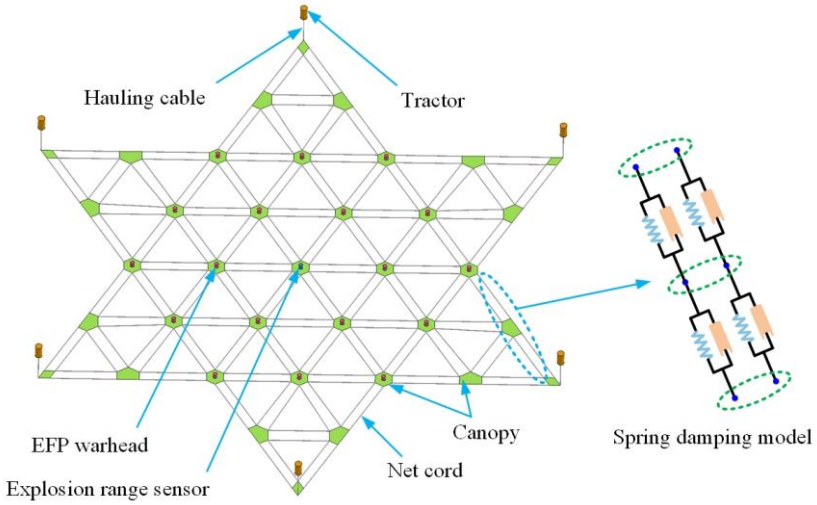

(**a**) Simplified diagram of space flexible web rope unit

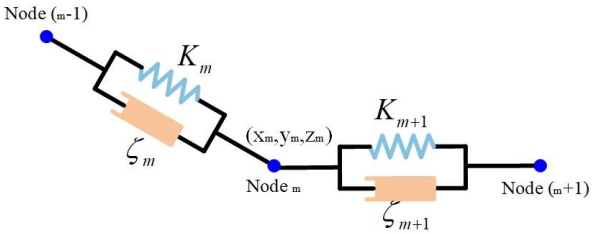

(**b**) Spring damping model diagram

Figure 6. Diagram of rope segment units.

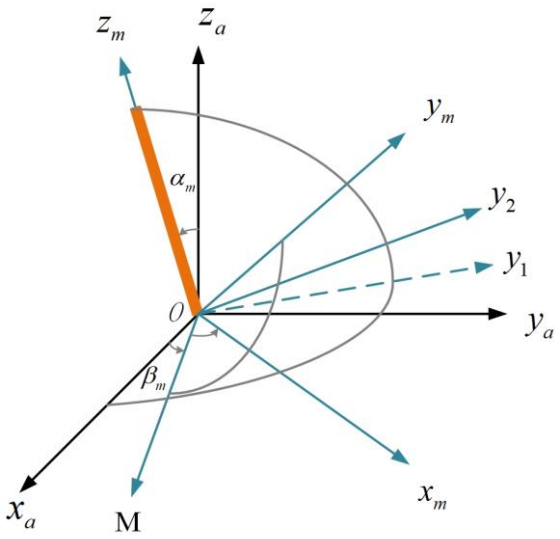

Figure 7. New spatial flexible web rope segment conversion coordinate system.

Because the web rope is soft, it can not bear ordinary bending moments and shearing force but can only bear tangential pulling force. Therefore, ignore Euler Angle χ_m, or

assume $\chi_m = 0$ and simplify the transformation matrix between the two coordinate systems as follows:

$$A_m = \begin{bmatrix} \cos\beta_m & \sin\beta_m & 0 \\ -\cos\alpha_m \sin\beta_m & \cos\alpha_m \cos\beta_m & \sin\alpha_m \\ \sin\alpha_m \sin\beta_m & -\sin\alpha_m \cos\beta_m & \cos\alpha_m \end{bmatrix} \tag{8}$$

In order to understand the whole calculation process more clearly, the variables and symbols involved in the calculation are summarized as shown in Table 1 below.

Table 1. Explanation of symbols and variable meanings.

Symbols (Variables)	Meaning
K_m	Spring stiffness of spring damping element
ζ_m	Damping coefficient of spring damping element
$Ox_m y_m z_m$	The jointed coordinate system of the flexible rope segment in the first space
$Ox_a y_a z_a$	Inertial coordinate system of the flexible rope segment in space
α_m, β_m, χ_m	Three independent angular parameters representing the position of a fixed point rotating rigid body are the rotation Angle, nutation Angle and precession Angle.
$p_m(\delta_m)$	Linear tension function of the nth segment web rope
μ	Tension damping coefficient of web rope
ε_m	Strain of web rope
$L_{m.0}$	The original length of the web rope
L_m	Length of web rope after deformation
$\dot{\varepsilon}_m$	Strain differentiation of net rope
g_m	Mass of flexible web rope segment
$G_{b.n}$	Normal mass matrix of rope segment
$F_{b.m}$	Normal fluid resistance of rope segment

Calculation of the Internal Force of Space Flexible Web Rope Segments

In general, because it is difficult to obtain the dynamic stress–strain relationship of the web rope, the static stress–strain relationship curve of the web rope is often used in engineering. Using segmented linearization, the constitutive relationship of the web rope is simplified into the sum of linear elasticity and linear velocity damping. That is, the tensile force of the m space flexible web rope segment is obtained by the following formula:

$$H_m = \begin{cases} \mu(\dot{\delta}_m) + p_m(\delta_m) & \delta_m > 0 \\ 0 & \delta_m \le 0 \end{cases} \tag{9}$$

In the above formula:
$p_m(\delta_m)$—Linear tensile function of the webbing rope in section m;
μ—Tension damping coefficient of rope segment of webbing unit;
strain ε_m is obtained by the following formula:

$$\varepsilon_m = \frac{L_m - L_{m.0}}{L_{m.0}} \tag{10}$$

$L_{m.0}$—Original length of web rope;

L_m—The length of the deformation is as follows:

$$L_m = \sqrt{(x_m - x_{m-1})^2 + (y_m - y_{m-1})^2 + (z_m - z_{m-1})^2} \tag{11}$$

The strain differential of the web cord unit can be obtained by differentiating the above:

$$\dot{\varepsilon}_m = \frac{(x_m - x_{m-1})(\dot{x}_m - \dot{x}_{m-1}) + (y_m - y_{m-1})(\dot{y}_m - \dot{y}_{m-1}) + (z_m - z_{m-1})(\dot{z}_m - \dot{z}_{m-1})}{L_{m.0} L_m} \tag{12}$$

Dynamical equation of spatial flexible web expansion system

If the mass of the space flexible rope segment is recorded as g_m, the mass matrix of the m space flexible rope segment is shown in the conjoined coordinate system as follows:

$$G_{b.m} = \begin{bmatrix} g_m + g_{a.m} & 0 & 0 \\ 0 & g_m + g_{a.m} & 0 \\ 0 & 0 & g_m \end{bmatrix} \tag{13}$$

The mass of the nth space flexible rope segment and $(m + 1)$ space flexible rope segment were divided in half and concentrated in the m space elastic rope segment by engineering approximation. The mass matrix at the node of the m space flexible rope segment is then represented by the inertial coordinate system:

$$G_m = \frac{1}{2}[A_m G_{b.m} A_m^T + A_{m+1} G_{b.m+1} A_{m+1}^T] \tag{14}$$

If the coordinate array of the fluid force $F_{b,m}$ in the connected coordinate system $Ox_m y_m z_m$ is denoted as $F_{b.m}$, the external forces $F_{b.m}$ and $F_{b.m+1}$ of the nth space flexible wire rope segment and the $(m + 1)$ space flexible wire rope segment are respectively added to the nth node by the engineering approximation method, therefore, the fluid force received at the nth wire rope segment node is expressed in the inertial coordinate system as:

$$F_m = \frac{1}{2}(A_m F_{b.m} + A_{m+1} F_{b.m+1}) \tag{15}$$

If the coordinate array of the pull Q_m in the nth space flexible rope segment under the connective coordinate $Ox_m y_m z_m$ is recorded as Q_m, the equation of dynamics at the node of the m space flexible rope segment is as follows:

$$G_m \begin{bmatrix} \ddot{x} \\ \ddot{y} \\ \ddot{z} \end{bmatrix} = A_{m+1} Q_{m+1} - A_m Q_m + F_m + G_m g \tag{16}$$

Acceleration at all nodes of the tether unit is obtained from the above (16), and then the acceleration of the entire intercept space flexible web is obtained.

5. Simulation Analysis of Traction Dynamics of the Space Flexible Web

Flexible web rollout is the crucial step in intercepting incoming targets. The traditional hexagonal webbing ejection is carried out by detonating charge, which leads the traction body to eject the flexible webbing ejected directly from the storage webbing launcher, and the overload of the webbing and incoming targets is used to entrap incoming targets. The deployment mode of the new space flexible web is realized by rifling common cavity firing. The firing pin triggers the primer to drive the propellant to detonate, and then the propellant is detonated. The six traction bodies are ejected from the launch inner tube. The six traction bodies fly under the action of centrifugal force to drive the deployment of the new space flexible web. The new space flexible web detonates the loaded EFP warhead

under the rising section's instantaneous "concave" web posture. It forms a high-energy jet to blast and intercept the incoming target.

5.1. Analysis of the Traditional Rope Web Unfolding Process

In the traditional rope web launching and deployment simulation model, the shape of the mesh body adopts a hexagonal structure of the same size as the new space flexible web; The hexagonal length is 2.5 m, the grid element is a conventional quadrilateral element, the unit is 0.4167 m $\times$ 0.4167 m, and the web rope is a circular cross-sectional flexible rope with a diameter of ϕ10(mm) , as shown in the figure in Figure 2 above. The flexible web rope is launched and pulled by six pullers, which are reduced to six cylinders with a diameter of 0.1 m and a height of 0.2 m on the bottom.

Because of the dynamic characteristics of sizeable nonlinear deformation of the mesh rope, the flexible mesh rope is set by LINK167-unit, considering that among the many element types such as BEAM, SHELL, and SOLID, the LINK167 unit [18] is similar to the spring-unit and is only subjected to axial tension. Improper selection of the unit type will lead to incorrect solution results. The initial model is the complete unfolded state of the figure in Figure 2 above, and then the initial unfolded state is changed to the specified receiving state by speed control. Because the folding process of the web rope is complicated and the web attitude of the receiving state is difficult to be characterized, we therefore simulate the receiving state of the actual web rope before launching, employing an instantaneous receiving attitude of the flexural rope movement under speed control, and then export the element information and nodal information of the model through the output command in LS-PREPOST processing, modify the K information of the initial fully extended model, and reset the initial emitting velocity to conduct a simulation. The model processing is shown in Figure 8 below.

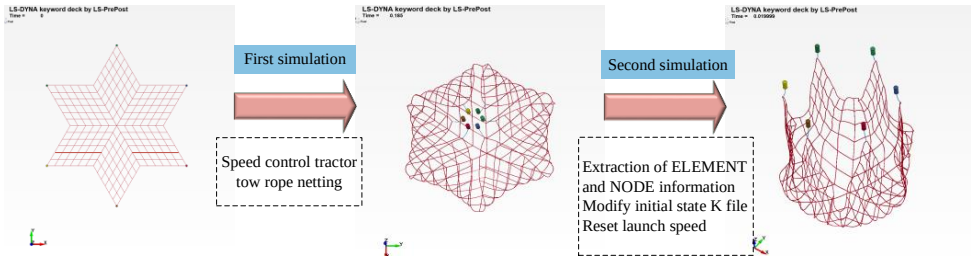

Figure 8. Process of traditional rope web simulation model.

After the model processing, 22,976 NODE messages were generated from the traditional rope web model in the receiving state. Gravity was set along the Z-axis, and air resistance was achieved by damping. These are considering that this chapter focuses on the simulation process of the traditional rope web, topological rope web, and a new type of space flexible web flying along the Z-axis, comparing and analyzing the dynamic characteristics of the new type of space flexible web. Therefore, the Z-direction launch initial velocity of six tractors is set to 50 m/s in line with the actual speed, and the X-direction and Y-direction are set separately according to the different positions of the six tractors, each tractor body's X- and Y-direction combined speed is 50 m/s so that the object can be formed in the air for a short period. The simulation run time can be taken into account in the study of the traditional roping deployment process.

In the finite element model of Figure 8 above, the traction body is set to rigid body PART, and the web rope is set to flexible body PART. The connection between the two is defined by the keyword *CONSTRAINED_EXTRA_NODESD. The parameters of the simulation material for the flexible web rope and the traction body are set out in Tables 2 and 3 below:

Table 2. Material parameters of flexible webs.

Type of Material	Density *RO*/(kg/m^3)	Elastic Modulus E/Pa	Poisson's Ratio *PR*
Kevlar Rope Material	1850	7.8×10^{10}	0.08

Table 3. Material parameters of traction body.

Type of Material	Density *RO*/(kg/m^3)	Elastic Modulus E/Pa	Poisson's Ratio *PR*
Tungsten Alloy	17,700	3.24×10^{11}	0.303

Due to the significant flexible deformation problem, the solution time of the model is long, and the non-convergence is easy to occur. After solving the problem, the simulation process of projectile deployment of conventional symmetric structure flexible mesh rope is shown in Figure 8 below. Figure 9a–h represent eight typical instantaneous poses during the unfolding of the rope net. It was observed that the rope web experienced about 0.12 s from the folding and receiving state to the expansion and forming of the rope to the maximum area.

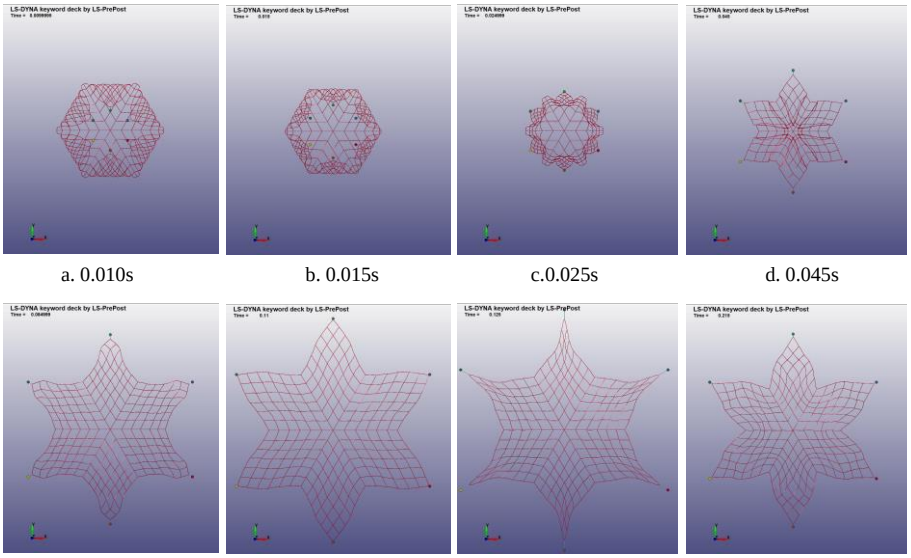

a. 0.010s b. 0.015s c.0.025s d. 0.045s

e. 0.085s f. 0.110s g. 0.125s h. 0.215s

Figure 9. Diagram of the general flexible web launch process.

According to the above traditional rope web ejecting process, mainly around the axial force of the rope web, rope deformation, and traction body (and web rope) of the movement of the analysis is shown in Figure 10 below, and diagrams a to f depict the forces on the webbing at six instantaneous moments. Because of the high initial launch velocity, the tractor rope attached to the six tractors was the first to receive traction. The axial tensile peak value of the entire tether was concentrated at the tractor at the start of the launch, and the maximum axial tensile value of the traditional tether web was 4.348×10^4 N at the bottom of the 0.155 s during the launch. As the rope webbing unfolds under the tractor, the force state changes and the web webbing unfolds in an undulating jittery state, as shown in c–e in Figure 10.

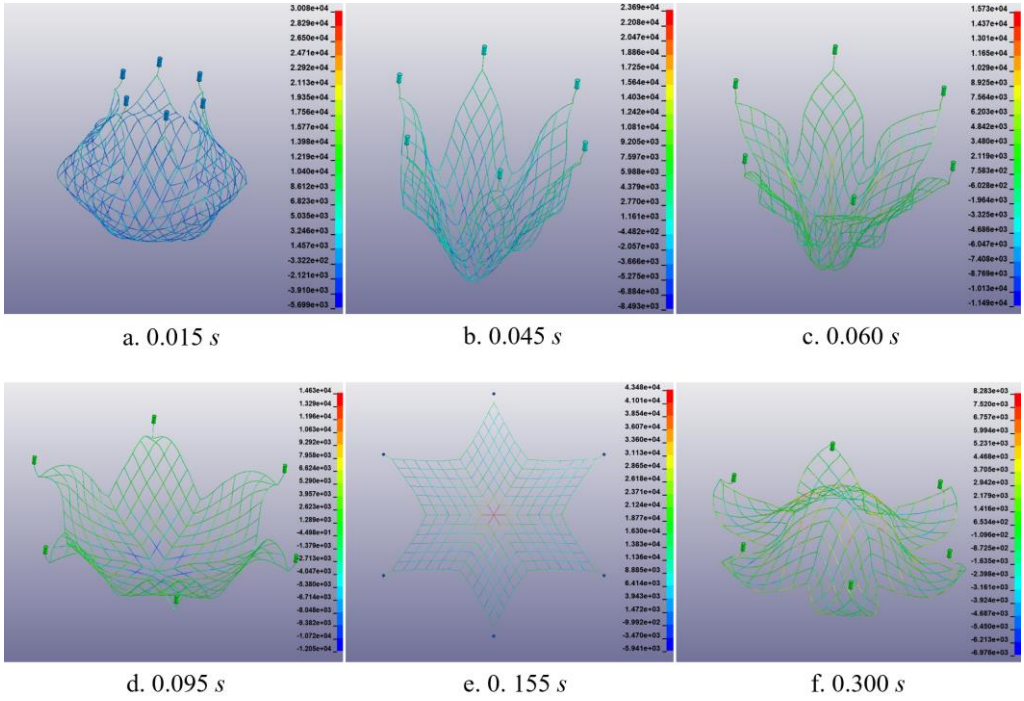

Figure 10. Axially loaded force of traditional rope line.

When the rope web is unfolded to the maximum area, the rope tenses, the traction body and the rope web shrink under the action of tension, the web surface appears slack, and the middle part of the rope force decreases, as shown in Figure 10f. The overall spread area of the rope web decreases gradually, and then after a short distance, the rope web loses its upward momentum and starts to fall under the action of gravity. In the unfolding process of the traditional rope web, the maximum deformation of rope segment elements at different positions of the rope web appears on the traction rope, and the maximum value is 4.267 m. The closer you are to the center of the regular bottom of the web, the less distortion there is.

In order to further explore the dynamic mechanical behavior of conventional flexible rope, the simulation results are analyzed by selecting the traction body feature points and four feature points of the traditional rope web. Figure 11 below shows the traction rope feature point A, the center feature point B at the bottom of the traditional rope web, the intersection point C of the outer line of the traditional rope web, and the internal feature point D of the traditional rope web are shown in Figure 11 below.

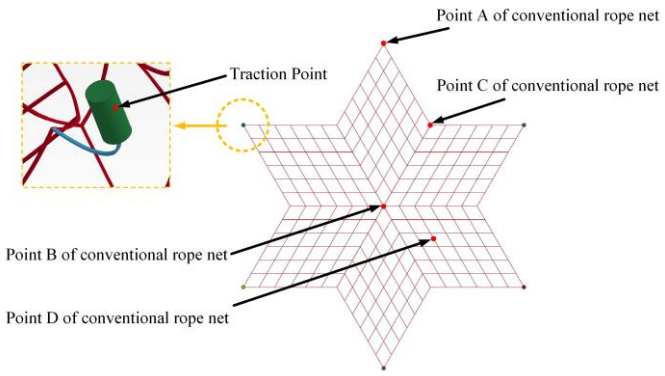

Figure 11. Characteristic point diagram of traditional rope web simulation analysis.

According to Figure a of Figure 12 below, an analysis of the corresponding velocity curve of traction body feature points, the initial towing speed is 71 m/s. Near the 0.14 s

moment, the towing speed decreases and then increases. Combined with the corresponding simulation process, rope webbing unfurls to the maximum area near the time. Under the action of axial tension between the rope lines, the traction body and rope web begin to shrink, and the speed of the traction body decreases. At this time, the speed of the rope web is greater than the speed of the traction body; moving it up the Z-axis, the velocity value of the traction body increases, and then the velocity value decreases gradually.

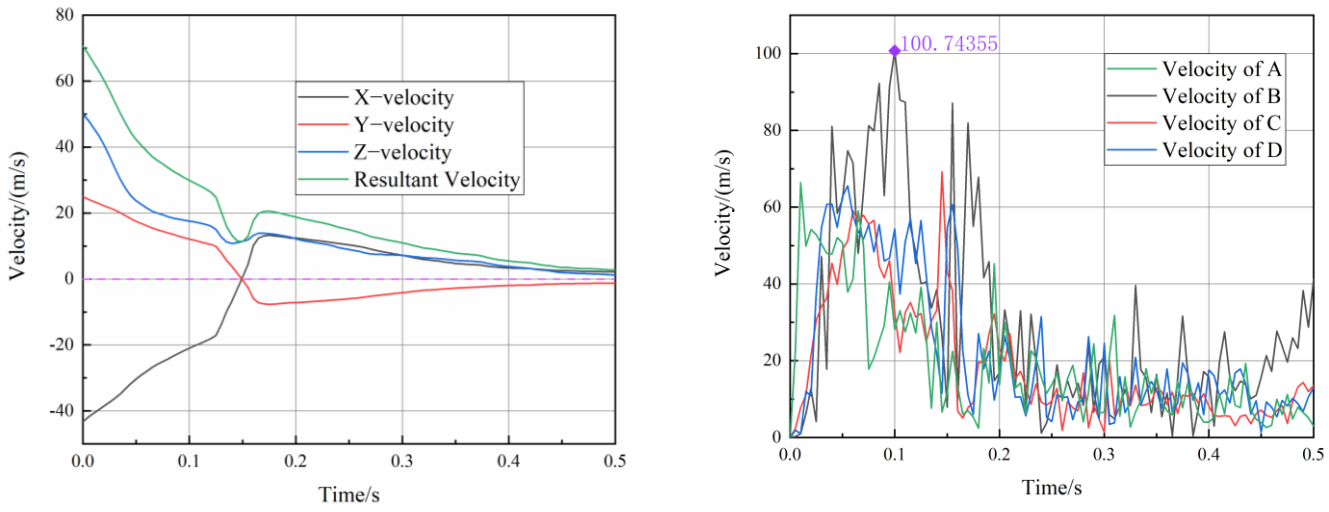

(**a**) Tractor velocity graph (**b**) Flexible web rope characteristic points velocity graph

Figure 12. Traditional rope web characteristic point velocity change graph.

As can be seen from the analysis of the b figure in Figure 12 below, the initial velocity at the four characteristic points of the traditional rope web is 0 m/s. After ignition and launch, the velocity of the points begins to increase sharply and oscillate constantly, and the general trend appears to increase and then decrease. Looking at the initial ascent of the A, B, C, and D four-point correspondence curves, we can see that the C-point correspondence curves rose the fastest, followed by D-points, and B-points rose the slowest. The maximum velocity of the four feature points appears at 0.09 s of the corresponding curve of the B-point, at which point the B-point velocity value reaches 100.74355 m/s. It can be seen from the simulation process in Figure 8 that this time is in the rising stage of the rope web ejection deployment. Now, the maximum size of the fully deployed web rope is near. The surrounding web rope drives the web rope near point B at the bottom of the rope to move up along the Z-axis. At this time, the speed value of the surrounding web rope starts to drop, and the peak value of the speed at point B lags behind other points of the rope web.

As shown in Figure 13 below, the initial displacement of the traction body is 0 m in all directions, and the displacement of the characteristic points of the traditional rope web increases gradually in the unwinding state, and the corresponding displacement of the characteristic points of the rope web increases in the order of distance from the traction body. According to an observation in Figure 13b, the bottom characteristic point B of the rope web corresponds to the Z displacement near 0.149 s, and a significant downward section begins from 7.066 m. Combined with the expansion process figure in Figure 9 above, the bottom central point B of the rope web moves to the top of the overall web rope. The tensioning of the web rope causes the displacement to decrease under the tensile force of the surrounding web rope, near 0.155 s. The characteristic point B of the web moves to the lower part of the overall web, and the displacement increases. With the decrease in the velocity of motion after ejection, the displacement curve change gradually flattened in the process of unfurling. According to the displacement curve, the altitude of the traditional rope web under this condition is 9.048 m. It is not difficult to observe the b-graph curve and find that in the maximum displacement during the test direction (Z-direction) expansion,

point B at the bottom of the rope web > point D inside the rope web > point C, where the outside line intersects > point A of the tow line.

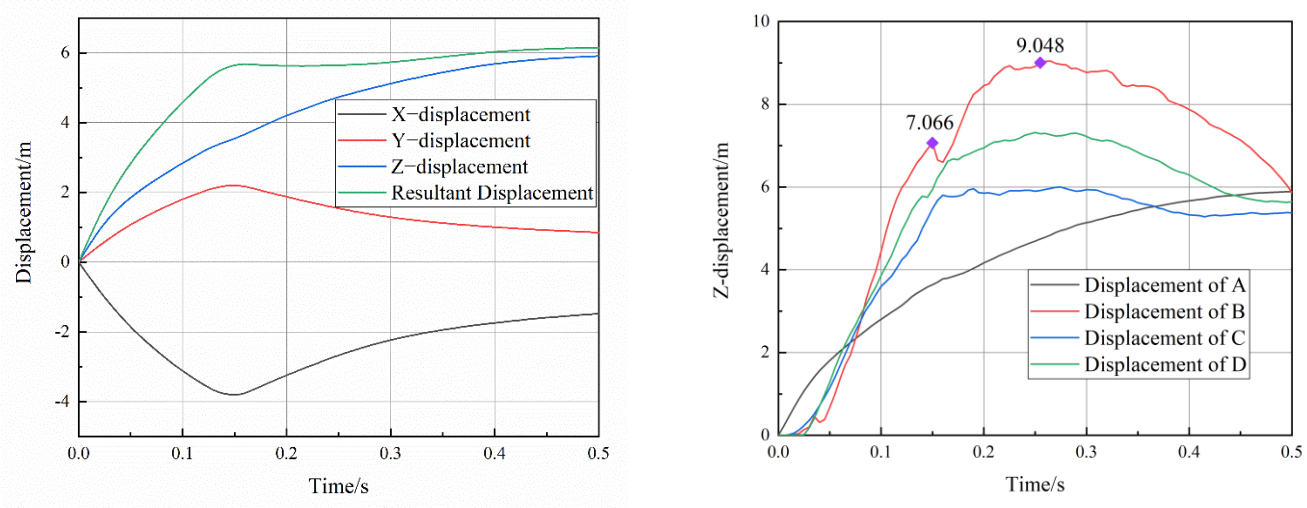

(**a**) Tractor displacement curve (**b**) Z-direction displacement curve of flexible web rope feature point

Figure 13. Change of characteristic point displacement of traditional rope web.

5.2. Analysis of Expansion Process of Topological Rope Web

In the pre-processing of the launch deployment simulation of the new space flexible web with the topological tether web (from now on referred to as the topological rope web), the same parameter settings are adopted as those of the conventional flexible rope web, including material model, element type and initial launch velocity, etc. The difference between the two is only in the form of a topological structure. When setting its firing muzzle velocity, the firing muzzle velocity of the six tracers in the Z-direction is set as 50 m/s consistent with the deployment of the traditional rope web. The combined velocity in the X-direction and Y-direction is set as about 50 m/s so that the research object can quickly be deployed and formed in the air.

Figure 14 below shows the initial attitude of the fully extended topological rope web simulation model output-related element and nodal information aftermath simulation model to simulate the reception attitude of topological rope webs in a storage grid launcher. The model contains 29,917 nodes and the parameters of the traction body are entirely consistent with those of the conventional web. The hexagonal side length is 2.5 m and the fully open area is about 32.48 m^2.

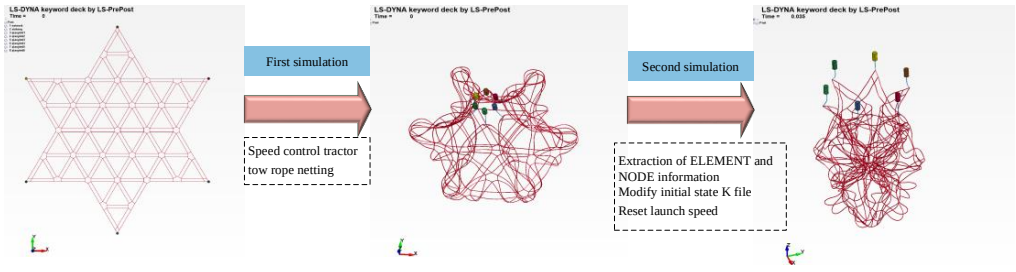

Figure 14. Process of topological rope web simulation model.

The expansion process of the topological rope web is shown in Figure 15 below, and Figure 15a–h reflect eight typical poses in the unfolding process. It is found that the attitude change of the topological rope web is similar to that of the traditional rope web in overall appearance and the time to reach the maximum unfolding area is about 0.14 s after launch, which is slightly later than that of the traditional rope web. By analyzing the posture of

the topology rope web at different times, it can be found that the deformation of the inner hexagonal topology element is smaller than that of the surrounding connection rope, which plays a specific role in supporting the stability of the local web type.

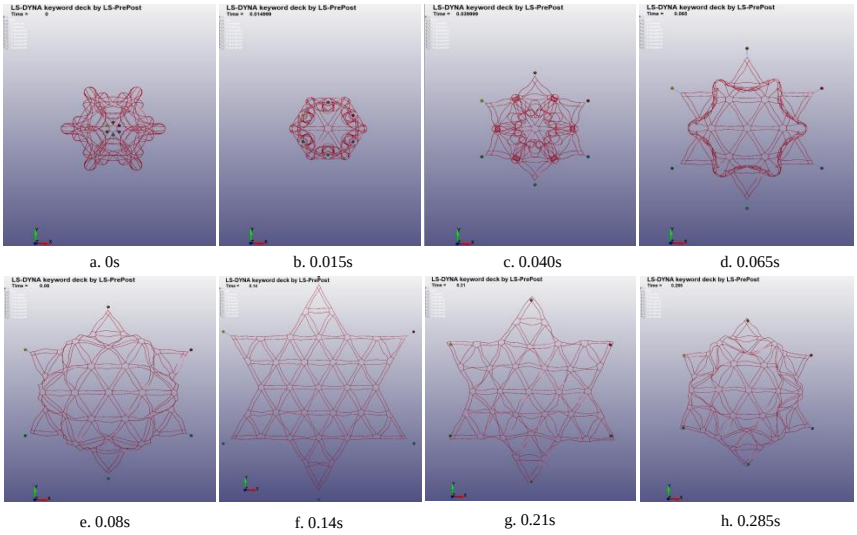

Figure 15. Map of topological rope web launch process.

As shown in Figure 16 below, the unfolding process of the topological rope web and the partial descent process after reaching the highest point are shown in Figure 16a–g. The tension changes of rope segments along the direction of rope segments at six different times are selected. As can be seen from the force cloud diagram at six representative moments, the tension of the rope segments showed a uniform change in the annular direction with the continuous unfolding and forming of the topological rope web along the *Z*-axis. Taking the geometric center at the bottom of the topological rope web as the reference point, the tension values of the rope segments showed a wave-like distribution law of "size staggered" along the radial direction. In the whole process of launching and unfolding the topological rope web, the maximum tension of the rope segment appears at the position of the rope segment on the traction rope at 0.140 s, which is about 7.254×10^4 N. At this time, the topological rope web is fully expanded or close to fully expanded, the rope segment is tensioned, and the axial force is higher than the other five typical moments.

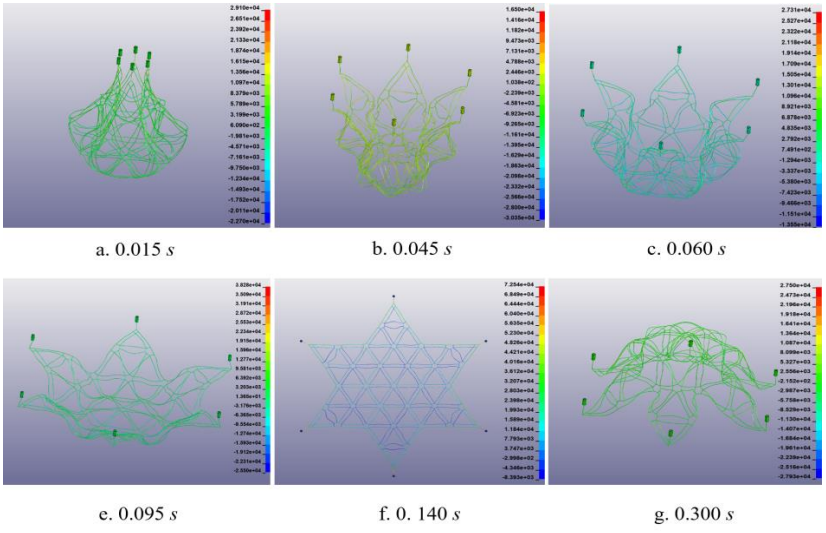

Figure 16. Axially loaded topological rope web segments.

In order to further discuss the dynamic characteristics of the topological rope web, the characteristic points of the traction body and four characteristic points of the topological rope web are selected to analyze the simulation results, as shown in Figure 17 below. The four characteristic position points of the topological rope web are the traction rope characteristic point A, the hexagonal edge line corner point B at the bottom of the rope web, the hexagonal edge line corner point C at the intersection of the outer edge line of the rope web, and the rope characteristic point D inside the rope web.

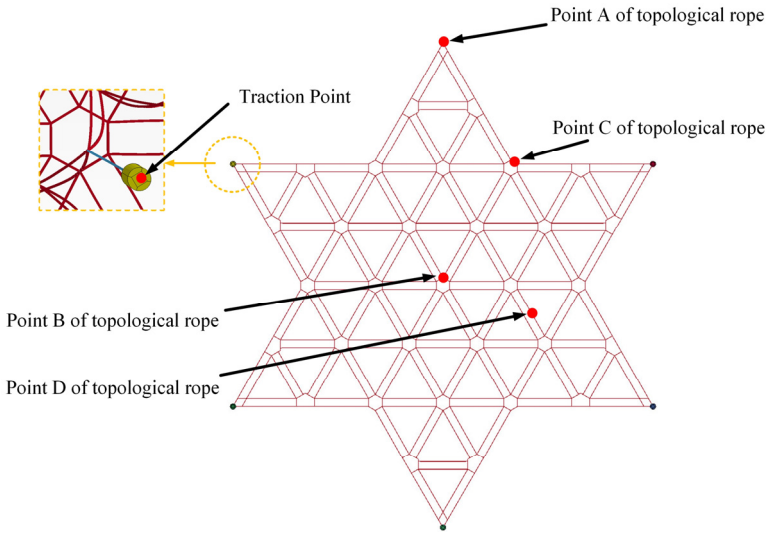

Figure 17. Topological rope web simulation analysis characteristic points diagram.

As shown in Figure 18 below, Figure 18a represents the velocity variation curve of the traction body in each direction during the launch and expansion process, Figure b shows the curve of the resultant velocity of four characteristic points of the topological rope web. Based on the analysis of the curve variation law in the figure, it can be seen that the initial velocity of the traction body is the same as the initial launching velocity set by the traditional rope web, which is 71 m/s. The initial velocity value of each characteristic point of the flexible rope in the topological rope web is 0 m/s. It is found that the velocity curve of the traction body in the X-, Y-, and Z-directions and the resultant velocity direction is the same as that of the traditional rope web. For the four characteristic positions of the topological rope web, the peak velocity appears at the bottom characteristic point position, reaching 116.132 m/s, which is higher than the peak velocity of the traditional rope web. In addition, when the 0.12 s flexible mesh approached or reached the maximum expansion area, compared with the traditional rope mesh, the vibration frequency and amplitude of the velocity curve of the topological rope mesh were lower than those of the traditional rope mesh, and the velocity curve corresponding to the bottom feature of point B is particularly pronounced. It can be seen that the structural stability of the topological rope web is better than that of the traditional rope web under the same working conditions.

As shown in Figure 19 below, in the topological rope web displacement change curve, the traction body's displacement change in the X-, Y-, Z-, and sum directions is consistent with that of the traditional rope web. According to the resultant displacement and Z-displacement in Figure a, in this case, the flying height of the traction body is about 5.7 m, which is slightly smaller than that of the traditional rope web. According to Figure b, it can be seen that the Z-direction displacements of points A, C, D, and B have changed successively, which also reflects the sequence of motion of each characteristic position of the rope web. According to the analysis of the a and b figures, compared with the traditional rope web, the maximum displacement of the traction body is the same within 0.5 s after launch, which is about 6 m. At 0.5 s, the traction body reaches the highest position, and the displacement of each feature point has entered the platform segment, which is in the oscillation process at the highest position. At this time, the displacement of the flexible

mesh rope is still rising gradually, and the deployed position is higher than the plane of the traction body point. The peak displacement of each characteristic point of the topological rope web is higher than that of the traditional rope web and the peak displacement of the bottom part of the topological rope web is nearly 12 m.

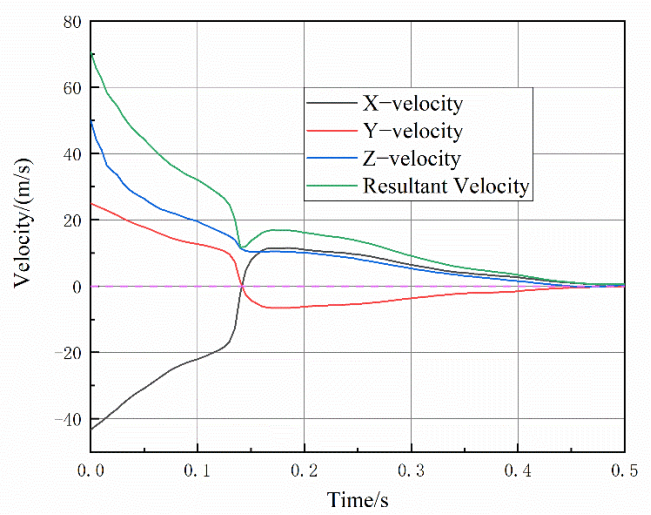

(**a**) Tractor velocity graph

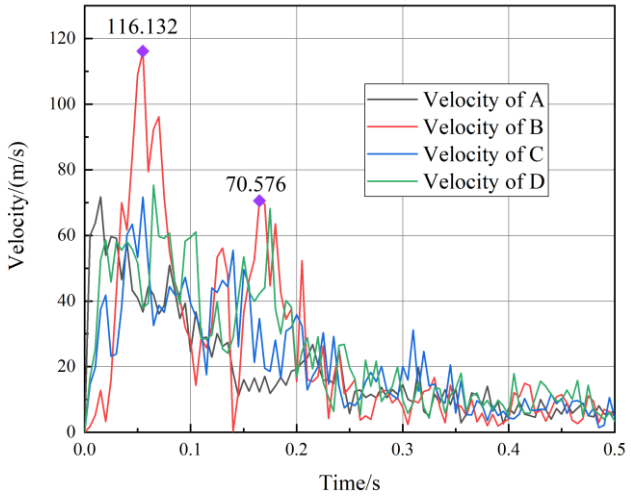

(**b**) Flexible web rope characteristic points velocity graph

Figure 18. Variation of velocity of topological rope web characteristic points.

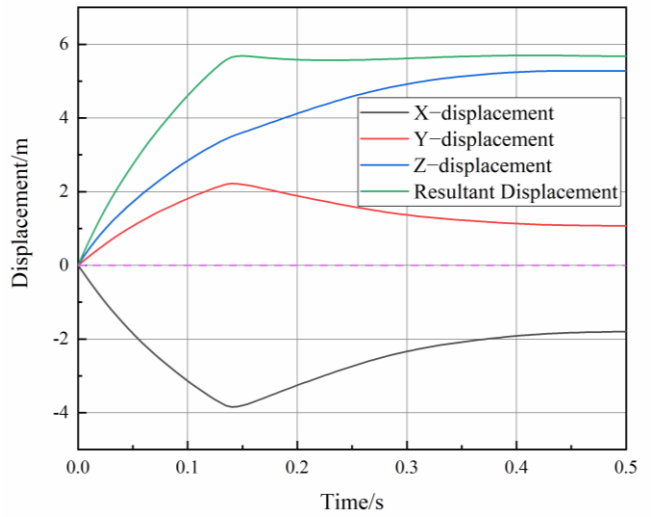

(**a**) Tractor displacement curve

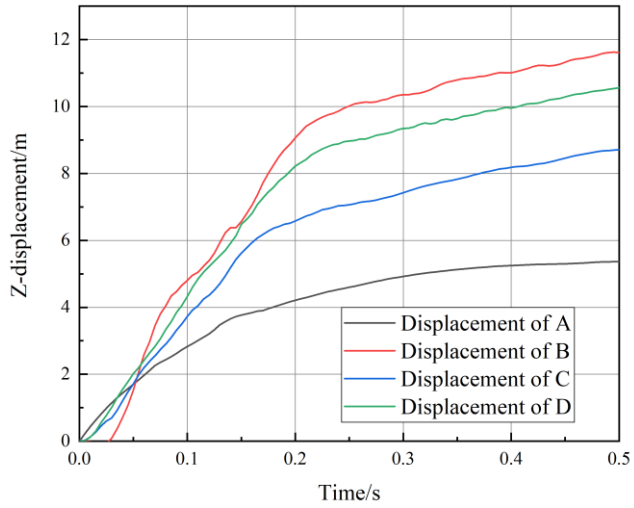

(**b**) Z-direction displacement curve of flexible web rope feature point

Figure 19. Topological rope web characteristic point displacement change diagram.

5.3. Analysis of the Expansion Process of New Space Flexible Web

A new space flexible web based on the principle of "shot blasting goal" interception, based on the topological rope web structure was improved. The web twine node connected by the canopy and the canopy fixed to the EFP high-energy warhead becomes a directional-shaped jet to hit the target to intercept. Because of the main research on the expansion of new space flexible web, the EFP warhead is replaced by a homogeneous aluminum alloy cylindrical rigid body, which is only considered the counterweight. Therefore, the modeling process is also different from the traditional rope web and topological rope web.

The topology structure and model processing of the simulation model of the new space flexible web expansion is shown in Figure 20 below. The outer part of the web adopts

a hexagonal structure of the same size as those above two pure flexible rope webs; the outer length is 2.5 m and the canopy adopts a regular hexagon with a side length of 0.14 m and thickness of 0.01 m. The size of the EFP warhead adopts a cylindrical structure consistent with the actual specimen, the diameter of the bottom surface is ϕ60(mm), the height is 66 mm, and the web rope is a flexible rope with a diameter of ϕ10(mm). In order to improve the flight stability of the new space flexible web, a double wire structure is used to connect the canopies, which is consistent with the topological rope web. The web rope of the new space flexible web adopts a LINK167 unit, consistent with the above two pure flexible rope webs. The canopies of the web rope node are represented by a SHELL unit, and the SOLID unit represents the EFP high-energy warhead.

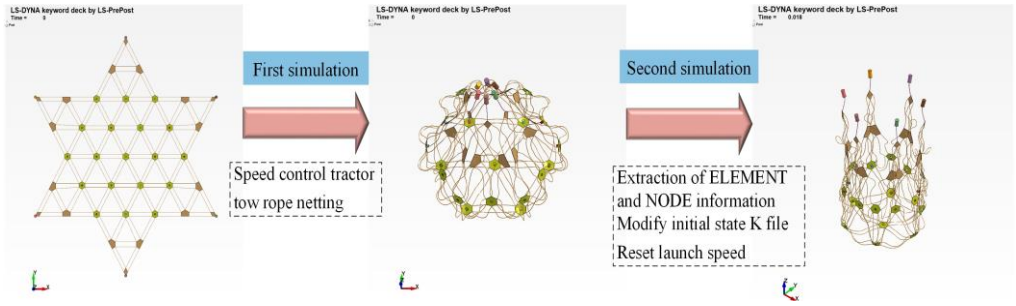

Figure 20. Process of simulation model of new space flexible web.

Regarding contact settings, the contact between the traction body and the wire and between the EFP warhead and the canopy belong to the connection between the rigid PART and the flexible PART. In the simulation model, some nodes on the wire are defined as particular nodes on the traction body using the keyword *CONSTRAINED_EXTRA_NODES. Similarly, some nodes on the canopy are defined as particular nodes of the EFP warhead. The connection between the canopy and the web rope is defined as the connection between flexible bodies.

The critical word *CONSTRAINED_NODAL_RIGID_BODY is used to bind the connection point of the web rope LINK167 unit and the nine points around the connection point of the umbrella SHELL unit and set it as the rigid node body. The preprocessing of the new spatial flexible web model is complicated, especially in the setting and control of the contact. An unreasonable setting will lead to the hourglass problem and negative volume.

After the establishment of the model by displacement control, the first process of the fully unfolded state of the new space flexible web in Figure 20 is simulated, folded into the storage state shown in the intermediate model, and then the unit and node information is extracted. After modifying the K file in the initial expansion state, the second process is simulated. The model contains 117,444 units. In addition to the above introduction, the parameter setting is consistent with the structure of the two pure flexible rope webs. The material parameters of the umbrella and EFP combat departments are shown in Tables 4 and 5 below:

Table 4. Canopy material parameters.

Type of Material	Density *RO*/(kg/m^3)	Elastic Modulus E/Pa	Poisson's Ratio *PR*
Kevlar Cloth	2000	9×10^{10}	0.08

Table 5. EFP combat material parameters.

Type of Material	Density *RO*/(kg/m^3)	Elastic Modulus E/Pa	Poisson's Ratio *PR*
Aluminium Alloy	2710	6.9×10^{10}	0.33

The simulation process of the expansion of the new space flexible web is shown in Figure 21 below, Figure 21a–h show eight typical poses in the process of "launch-unfold-fully unfold-partial retracement of the web." According to Figure 21a–f, it takes about 0.162 s for the new space flexible web to go from its folding storage state to unfolding to the maximum area. The unfolding time is longer than the two pure flexible rope web structural models above. By observing the detailed structural features of the new type of space flexible web at different moments, it was found that the existence of an umbrella coat unit can improve the flatness and stability of the local rope web structure of the new space flexible web, which plays a vital role in the rope support and the fixation of the EFP warhead.

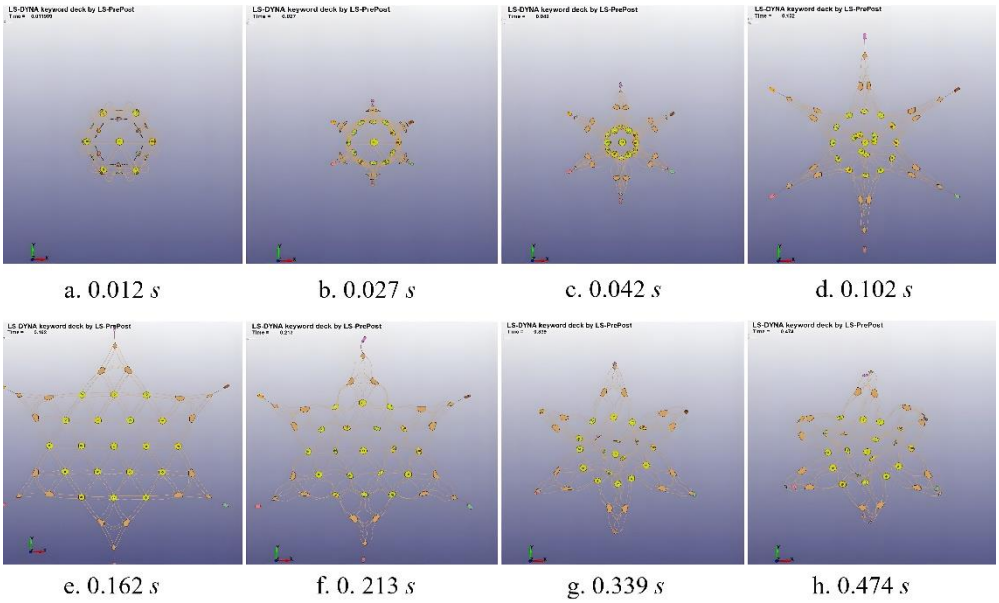

Figure 21. Sketch of the expansion process of the new flexible space web.

Observation of Figure 22 shows that in the expansion process of a new type of space flexible web, the force of radial web twine is more significant than ring web twine, and early on, most of the ring web twine is in a flabby condition. The axial tension peak of the new space flexible web continuously circulates in the radial mesh according to the law of "upper mesh rope–lower mesh rope–upper mesh rope." By analyzing the tension cloud diagram, it can be seen that when the deployed area of the rope web reaches 86% of the maximum open area, the axial tension value of the overall circular mesh is gradually greater than that of the radial mesh. The maximum tension value of the rope segment of the new spatial flexible mesh appears at the position of the traction rope at 0.171 s, which is about 5.113×10^4 N, and the peak time is later than that of the traditional rope web and the topological rope web. The overall variation law is consistent with the two pure flexible mesh rope structure models. Moreover, due to the high velocity in the XY plane, the EFP warhead, the canopy, and the web rope in the middle of the ring are squeezed in the radial direction with the force transfer between the web ropes during the launch and lift off.

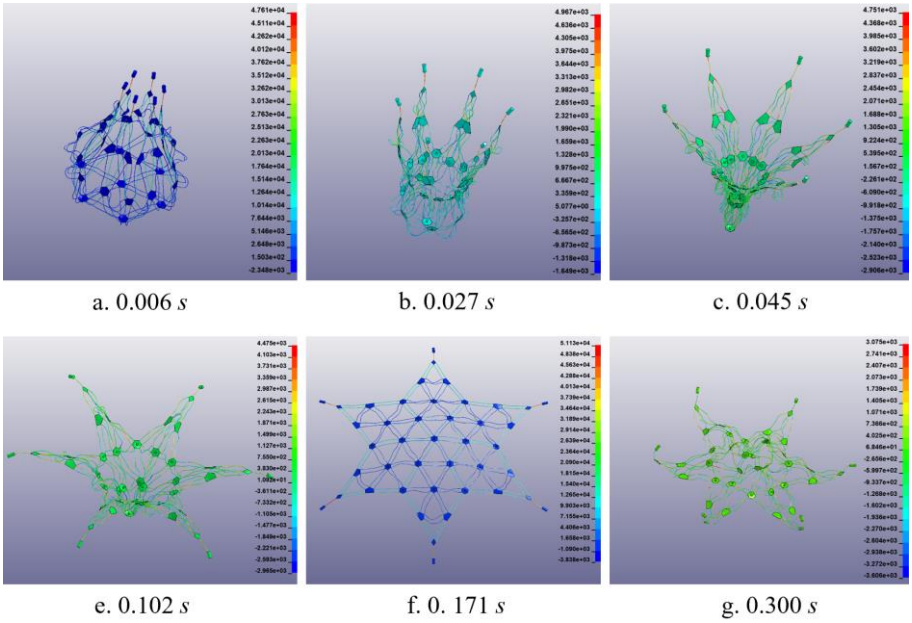

Figure 22. Axial load of the new space flexible web rope segment.

The dynamic characteristics of the traditional rope web and topological rope web are compared and analyzed. A total of five characteristic points of the traction body and a new space flexible web interception unit are selected to analyze the simulation results, as shown in Figure 23 below. Among them, the four feature points of the new space flexible web are the traction rope feature point A, the hexagonal edge line corner point B at the bottom of the EFP, the hexagonal edge line corner point C at the intersection of the outer edge line of the rope web, and the rope inside the rope web feature point D.

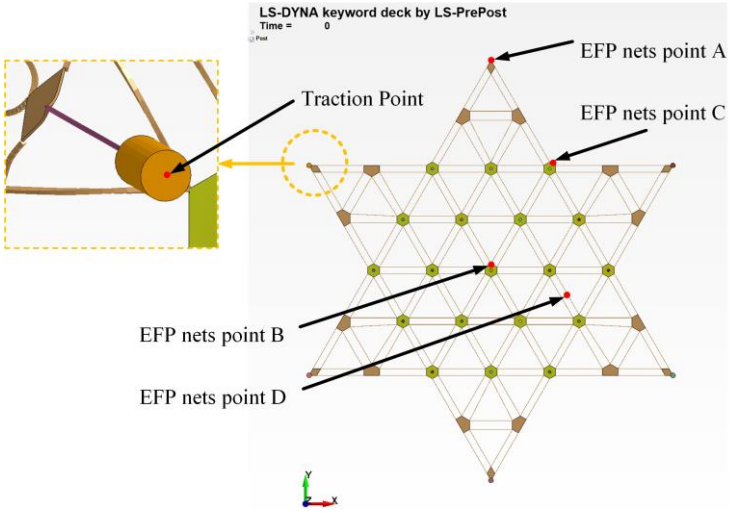

Figure 23. Characteristic point diagram of new space flexible web simulation analysis.

As shown in Figure 24 below, the velocity values of the three directions of the traction body X, Y, and Z are 43.3 m/s, 25 m/s, 50 m/s, respectively, and the resultant velocity of the three directions is 71 m/s. The variation trend of the velocity curve of the traction body is consistent with the traditional rope web and topological rope web mentioned above. Since the main body of the rope web of the new space flexible web is directly connected to the traction body through the traction rope, the movement of the EFP rope segment unit and the change of the web type will affect the speed change of the traction body during

the expansion process. Compared with the traction body, the development process of the velocity value of the flexible web is messy during the unfolding process of the new space flexible web. After the initial steep increase in each characteristic point of the flexible web, the overall trend of the velocity value of the flexible mesh is decreasing. By observing Figure 24b, it can be seen that the characteristic points at the bottom of the new space flexible web experience a steep increase at 0.06 s, and the maximum velocity of 103.988 m/s appears at 0.162 s. Combined with the unfolding process of Figure 21, it can be seen that at this time, the new space flexible web is approaching the time of complete unfolding, and the mesh rope is also oscillating from inside to outside. At this point, the bottom feature B is "swung" to the peak velocity by the surrounding mesh rope.

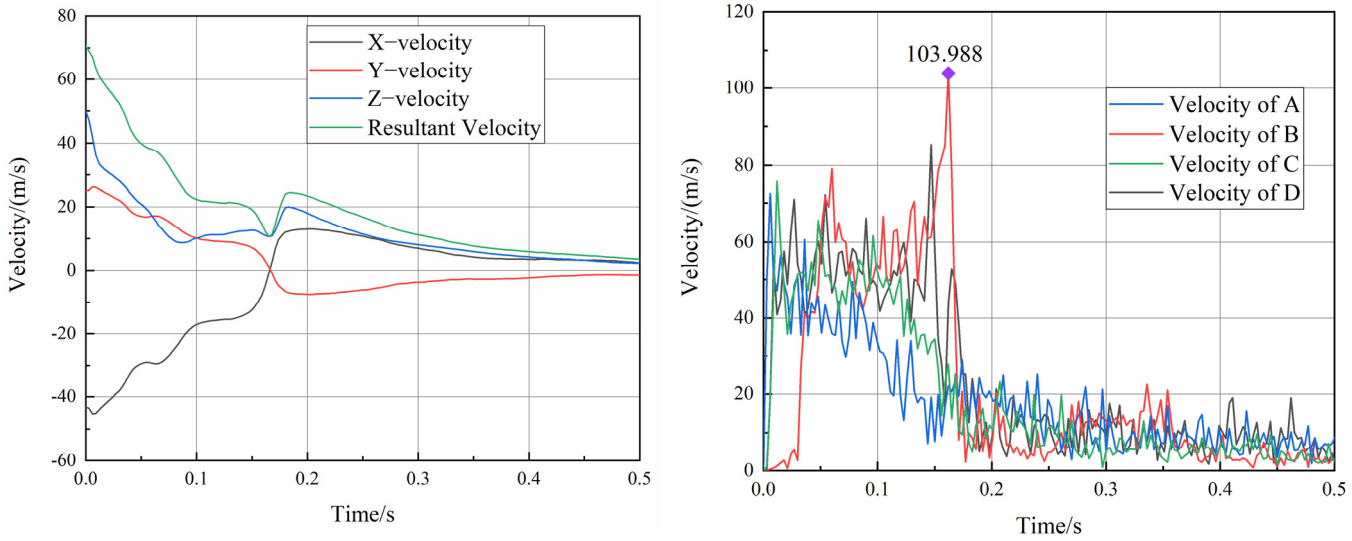

(**a**) Tractor velocity graph (**b**) Flexible mesh rope characteristic point velocity graph

Figure 24. Velocity variation of characteristic points of new space flexible webs.

According to the analysis of Figure 25 below, in the displacement change curve of the new space flexible web, the displacement changes of the traction body in the X-, Y-, Z- and resultant directions are consistent with those of the conventional web. According to the Z-displacement in Figure a, the flight height of the traction body under this condition is 5.62 m, which is smaller than that of the traditional rope web and higher than that of the topological rope web. However, the three are close to each other. According to Figure b, it can be seen that the displacements of points A, C, D, and B have changed successively, which also reflects the sequence of motion of each character's position on the rope web. According to Figure 25b, the flight height of the rope at the bottom of the new space flexible web > the inner rope > the edge rope > the traction rope. It can be seen that when the new space flexible web reaches the highest position in the air, the web bomb as a whole presents an upward bulging "convex" posture, and the maximum flight height is 9.028 m.

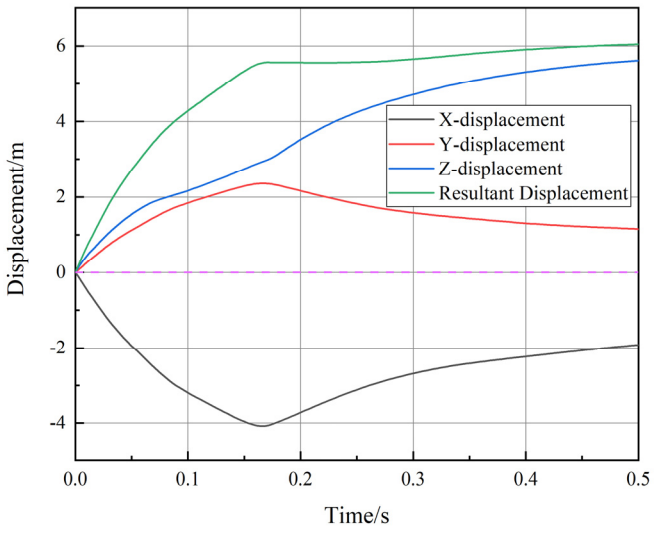

(**a**) Tractor displacement curve

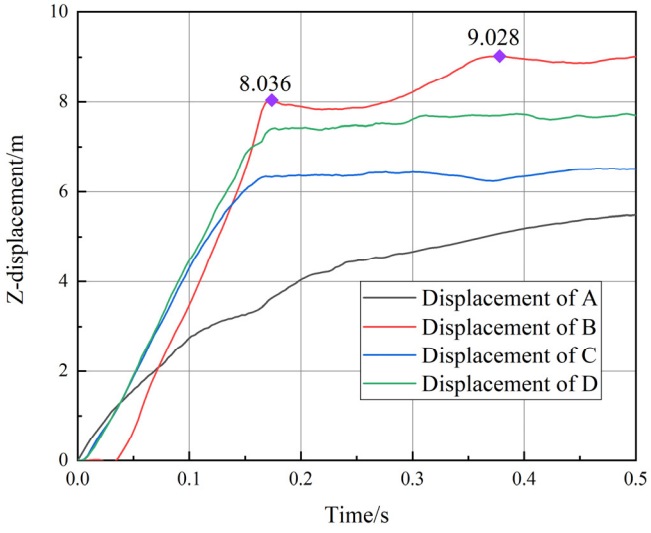

(**b**) Z-direction displacement curve of flexible mesh rope characteristic point

Figure 25. Change of characteristic point displacement of new space flexible web.

5.4. Simulation Comparison Analysis

By observing traditional rope web, topology rope web, and new space flexible web in the Z-direction displacement and speed curve of flexible web twine we found that spread and velocity in the process of three kinds of flexible web peak displacement are at the bottom of the web feature point B, therefore, the B points near the exact location of the unit were analyzed, and the rope tension variation curve is shown in Figure 26, as follows:

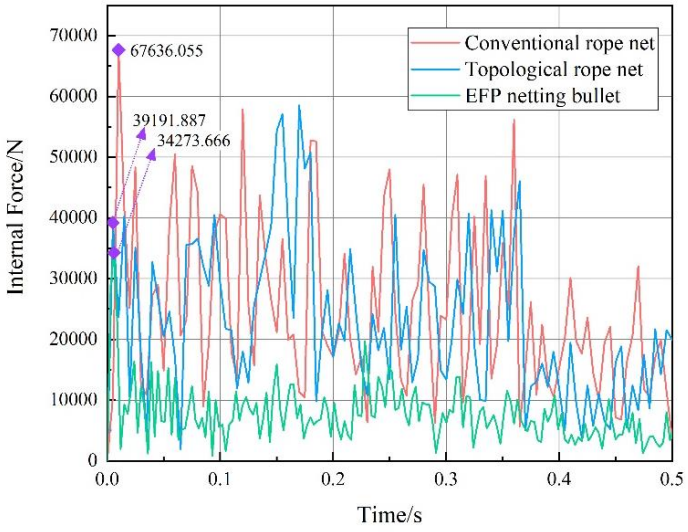

Figure 26. Tension curves of the bottom rope segments of three flexible rope webs.

By analyzing the rope segment tension curves in Figure 26, it can be seen that all three kinds of rope webs present irregular oscillatory changes. The rope segment tension amplitude of traditional rope webs is >topological rope webs >new space flexible webs. The maximum tension of traditional rope webs is 67,636.055 N, while that of topological rope webs is 39,191.887 N. The maximum tension of the rope segment of the new space flexible mesh is 34,273.666 N.

Rope webs with three different flexible structures are typical multi-body systems that experience a large range of motion and large deformation coupling, and the internal

constraints of the systems are complex. After the initial speed of the traction body is set, the unfolding process of the flexible rope web in the air is uncontrolled. By comparing and analyzing the dynamic evolution process of the traditional rope web, topological rope web, and new space flexible web, the following conclusions can be obtained:

(1) In terms of the unfolding time of the rope web, the unfolding time of the conventional flexible rope web is about 0.12 s, and the unfolding time of the topological rope web is about 0.14 s. The unfolding time of the new space flexible web is longer than the above two kinds of flexible rope webs. In the example, the new space flexible web needs about 0.162 s from the beginning to the entire unfolding state. It indicates that the new space flexible web has a longer time to maintain the "concave" posture suitable for interception than the traditional and topological rope webs and has better shape preserving property. In the actual process of intercepting the incoming target, the new space flexible web intercepts the space–time window more significantly, and the fault tolerance rate is higher.

(2) In terms of the traction body and the motion of the flexible web, the topological structure of the new space flexible web is similar to that of the topological rope web. The displacement of the two webs is more significant than that of the conventional flexible web, and the flight height of the two webs is higher, up to 11.624 m. In addition, under the same simulation parameter settings, the displacement of the topological rope web and the new space flexible web is at a slowly rising plateau before 0.5 s, when the traditional rope web has begun to fall significantly.

(3) In the changing aspect of the web type of the rope web, as a kind of flexible rope web with a more complex structure, the new type of space flexible web changes evenly during the expansion process, and the new type of space flexible web has the same jitter expansion rule as the traditional rope web and topological rope web, no web twine coil, and mixed and disorderly phenomena occurred. The new type of space flexible web canopy on the stability of the web type and EFP warhead fixed support play an important role as it can ensure that the EFP warhead can intercept the incoming projectile body in an optimal posture under the appropriate space–time window.

(4) As for the rope segment tension of the rope web, according to Figure 26, the rope segment tension amplitude of the new space flexible web is much smaller than that of the traditional rope web and the topological rope web, and the average rope segment tension is around 7500 N, which is also smaller than that of the other two kinds of rope web, indicating that the new space flexible web structure has good mechanical properties.

6. Simulation and Experimental Comparison of New Flexible Web

6.1. Testing of a New Space Flexible Web for Ground Launch

The new type of flexible space web is a typical nonlinear and large deformation multi-flexible coupling structure with vast application space in practical engineering practice. Due to its complexity in a low-altitude aerodynamic environment, only numerical analysis results are used to analyze its air deployment performance, which has a specific reference value, but the reliability is not good. Therefore, a ground launch and deployment test of the new space flexible web is carried out to compare and verify the simulation model and analysis results of the new space flexible web and further clarify its traction and expansion characteristics.

The schematic diagram of the setting and positioning of the test site is shown in Figure 27. The picture taken by a high-altitude UAV is used to illustrate the setting of the site. The figure shows the launching points of the new space flexible web, the erection positions of two high-speed stereo cameras, and four target positioning points. Before the test, the stereo camera was positioned, its field of view was adjusted, and its internal and external orientation elements were adjusted. After the calibration, relevant test measurements were recorded.

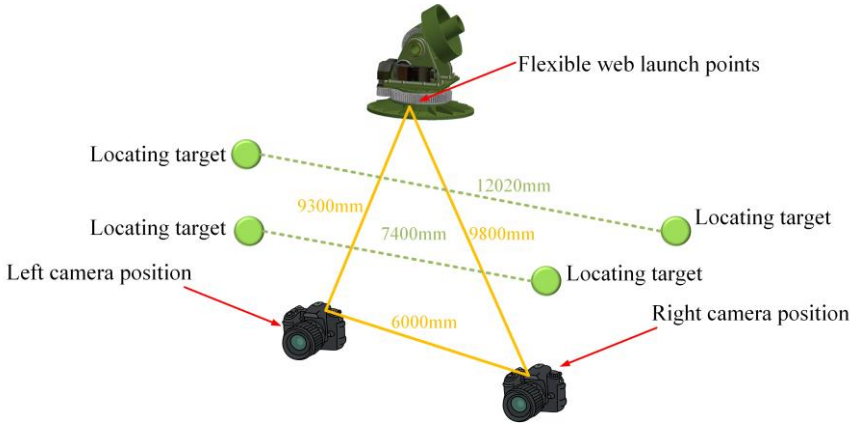

Figure 27. Location diagram of test site.

The experimental fuel adopts a 20 g double-base propellant, an electrical signal controls the charge initiation, and the new space flexible web is folded in the storage cage. In the ignition process, the internal energy of the charge is constantly transformed into the kinetic energy of the traction body, and six tungsten steel traction bodies are used to pull the new space flexible web to fly in the air. To visually express the measurement results, the measurement points of the new space flexible web are numbered, and the specific positions are shown in Figure 28 below.

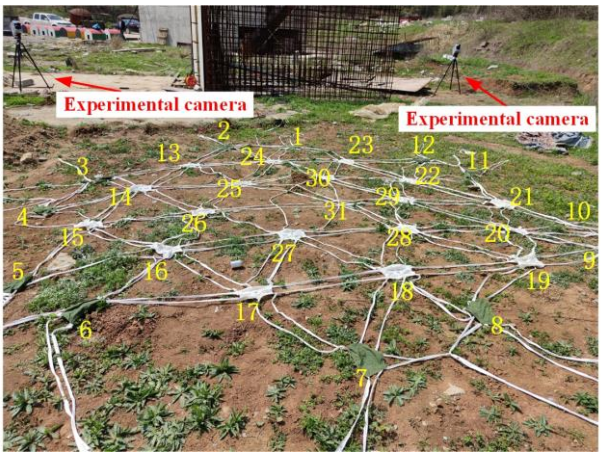

Figure 28. Numbering diagram of new space flexible web physical measurement points.

With ignition after launch, under the action of the traction force, the new flexible space web is gradually pulled and expanded from the ground storage box, molding in the air. When the web rope has tension, the traction body in the web tension retracts, the web surface relaxes, the overall expansion area is reduced, and then, in the rise of a short distance, the web rope loses upward power under the action of gravity and begins to fall. The whole test process is then complete. The new space flexible web is in the launch ascent stage from 0 to 2.75 s and the free fall stage from 2.75 s to 5.79 s. Figure 29 below shows the instantaneous air attitude changes of the new space flexible web at the selected characteristic moments in the whole test process. It is found that due to the influence of air resistance and transverse wind, the flight trajectory of the new space flexible web does not rise and fall in the vertical direction entirely, and a certain degree of deviation occurs in the established trajectory.

Figure 29. Timeline of air attitude change in the new spatial flexible web.

6.2. Comparison of Experimental Results and Simulation

The grid posture at representative moments in the test process is selected and compared with the simulation results in Section 5 above. The comparison diagram of the new spatial flexible grid configuration between the test and simulation is shown in Figure 30 below.

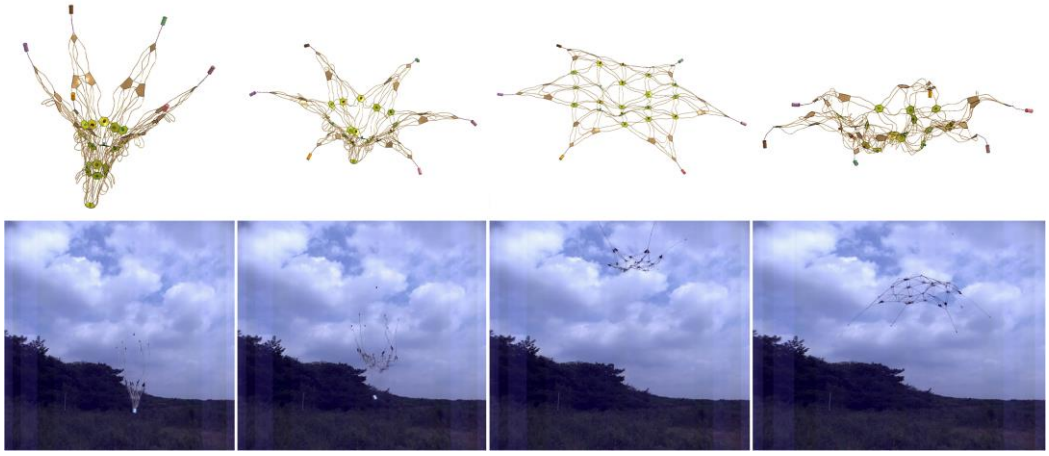

Figure 30. Comparison of new space flexible web experiment and simulation shape under feature moments.

Rising in the initial stage, the web twine mutually squeezing phenomenon is evident. The early new space flexible web attitude changes fast when achieving the maximum expansion area, the tractor body is restrained by the new space flexible web twine, the web twine tensions rapidly with new space flexible web prominent body structure retraction, and the web surface expansion area decreases rapidly. After continuing to rise for a short distance, the new space flexible web loses its rising power, falls back rapidly, and the effective deployed area also decreases rapidly. After comparing the test and simulation, it is found that the maximum effective deployment area achieved in the actual test process is smaller than the simulation value, and the mesh holding time in the test is also shorter than the simulation value, which is mainly affected by the inconsistent air resistance between the test and simulation.

As can be seen from Figure 31, the maximum value of vertical displacement of the new space flexible web in simulation and test is about 20 m, and the simulation value is slightly higher than the test value. The maximum vertical displacement time in the simulation of the new space flexible web is about 2.51 s, peaking earlier than the test results. Values can be found by looking at the flexible web actual test launch of the new space, its displacement peak near the end of the changes is flat, where there are about 1.3 s as the platform.

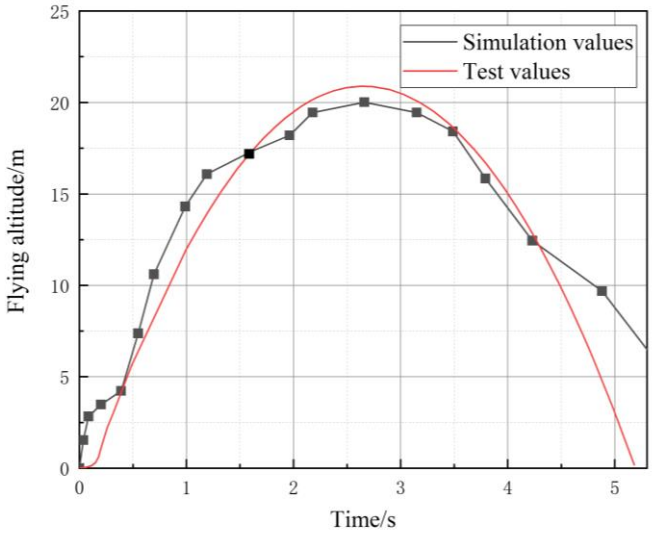

Figure 31. Changes of flight altitude of new flexible space web.

The ground test is in good agreement with the simulation results. The effective expansion area of the new space flexible web can reach more than 80% of its maximum size in the air, and the maximum flight altitude error is controlled by 5%. These results show that the new space flexible web has better flight ability in the air.

In addition to the observation of Figure 30, it can be seen that after 4.2 s, the test value and the simulation value show a significant deviation. This is mainly due to two reasons. On the one hand, the influence of air resistance and other conditions is not considered in the simulation. The launch is only affected by gravity, which is an ideal working condition. However, there is the effect of air resistance during the experiment. On the other hand, in the second half of the test, the wind slowed down the landing process of the flexible web. This also leads to a difference between the test and simulation values simultaneously.

During the launch and deployment process of the flexible web, the current verification test net size is relatively small, the flight range is close, and the intercept and capture target is mainly stationary or at low speed [19,20]. The simulation and verification tests of the new symmetrical structure flexible web make up for the above shortcomings and provide a new idea for the research. During the test, the flight height can reach tens of meters and the opening area can reach about 20 square meters.

7. Conclusions and Future Work

Based on the UAV interception's mission background requirements, a new space flexible web short-range interception method is proposed, which is different from the existing rope web structure. A simple example introduces the geometric nonlinearity of the flexible wire rope system. According to the flexible characteristics of the three types of webs, the unfolding dynamical model of a flexible space web is established. The traction deployment performance of the new space flexible web is verified through the simulation and comparative analysis of three flexible webs with different structures. Based on the established dynamic model, through the comparison of simulation and ground tests, the web posture, effective deployment area, and related forces in the process of

traction deployment of the new space flexible web are further analyzed, and the following conclusions are drawn.

The spatially symmetric flexible web has shown excellent performance in the field of UAV interception. This new flexible web structure has the advantages of a sizeable unfolding area, is fast forming, lightweight and low cost. The above benefits mean this structure could be more widely used in the field of interception and capture. Flexible mesh rope is a typical nonlinear and large deformation multi-flexible coupling object. The established theoretical model can only partially characterize the elastic characteristics of elastic web rope, which should be further improved. In addition, due to the test launch's high initial velocity and the web rope's significant flexibility, the measurement methods that can be used in the flexible web launch test are limited. Therefore, the change process of the web attitude is mainly studied and the flight height and other parameters are analyzed. The next step is to conduct more in-depth simulation and experimental research on the UAV interception process.

Author Contributions: This is a joint work and the authors were in charge of their expertise and capability: Y.L.: investigation and analysis; Z.X.: validation and revision; Y.Q.: methodology; F.Y.: writing and revision; C.M.: manuscript revision. All authors have read and agreed to the published version of the manuscript.

Funding: This research was supported by the National Natural Science Foundation of China's Major Research Instrument Development Project, grant number 51527810.

Data Availability Statement: The data used to support the findings of this study are available from the corresponding author on request.

Acknowledgments: The authors would like to express their gratitude to all those who helped them during the writing of this paper and the authors would like to thank the reviewers for their valuable comments and suggestions.

Conflicts of Interest: The authors declare no conflict of interest.

References

1. Rashid, E.; Ansari, M.D.; Gunjan, V.K.; Ahmed, M. Improvement in Extended Object Tracking with the Vision-Based Algorithm. In *Modern Approaches in Machine Learning and Cognitive Science: A Walkthrough*; Studies in Computational Intelligence; Gunjan, V., Zurada, J., Raman, B., Gangadharan, G., Eds.; Springer: Cham, Switzerland, 2020; Volume 885.
2. Huang, L.; Jiao, W.; Liu, G.; Sun, Y. *Design of Track Fusion System for Anti-Aircraft Gun Fire Network System[C]//3rd International Conference on Mechatronics, Robotics and Automation*; Atlantis Press: Dordrecht, The Netherlands, 2015; pp. 943–946.
3. Djurkovic, V.; Milenkovic, N.; Trajkovic, S. Dynamic Analysis of Rockets Launcher. *Teh. Vjesn.* **2021**, *28*, 530–539.
4. Cieślak, E. Unmanned Aircraft Systems: Challenges to Air Defense. *Saf. Def.* **2021**, 1. [CrossRef]
5. Wu, J.; Liu, J.; Du, Y. Experimental and numerical study on the flight and pewebration properties of explosively-formed projectile. *Int. J. Impact Eng.* **2007**, *34*, 1147–1162. [CrossRef]
6. Li, J.Y.; Yu, Y. Projecting Parameters Optimization for Space Web Systems. *J. Astron.* **2012**, *33*, 823–829.
7. Yu, Y.; Baoyin, H.-X.; Li, J.-F. Modeling and simulation of the projectile dynamics of space flight webs. *J. Astronaut.* **2010**, *31*, 1289–1296.
8. Zhai, G.; Qiu, Y.; Liang, B.; Li, C. On-orbit capture with flexible tether–web system. *Acta Astronaut.* **2009**, *65*, 613–623. [CrossRef]
9. Cheng, W.; Tianxi, L.; Yang, Z. Grasping strategy in space robot capturing floating target. *Chin. J. Aeronaut.* **2010**, *23*, 591–598. [CrossRef]
10. Fernandez, J.C.J.; Castanon-Jano, L.; Alonso, A.G.; Blanco-Fernandez, E.; Fernandez, J.C.G.; Gonzalez, V.C.; Castro-Fresno, D.; Garcia-Sanchez, D. 3D numerical simulation of slope-flexible system interaction using a mixed FEM-SPH model. *Ain Shams Eng. J.* **2022**, *13*, 101592. [CrossRef]
11. Xu, B.; Yang, Y.; Yan, Y.; Zhang, B. Bionics design and dynamics analysis of space webs based on spider predation. *Acta Astronaut.* **2019**, *159*, 294–307. [CrossRef]
12. Chen, Q.-Q.; Feng, Z.-W.; Zhang, G.-B.; Wang, X.; Zhang, Q.-B. Dynamic Modeling and Simulation of anti-UAV Rope Web Capture System. *J. Natl. Univ. Defense Technol.* **2022**, *44*, 9–15.
13. Zhou, Z.W.; Cheng, C.; Zhang, X.B.; Bian, W. Numerical Simulation and optimization of launching process of anti-UAV web catcher. *J. Ballist.* **2019**, *31*, 1–6.
14. Liu, H. *Dynamics and Control of Space Rope Web Deployment and Complex Deorbit [D]*; National University of Defense Technology: Changsha, China, 2014.

15. Zhang, Z.; Qian, Q.; Wang, J.; Liu, H.; Liang, K.; Li, Z.; Liu, G. Study of Passive Protective Web Protecting the Rockfall Caused by Open-Pit Blasting on High and Steep Slope. *Shock Vib.* **2021**, 4577889.
16. Lu, Y.; Rong, W.; Wu, S. Dynamic characteristics simulation analysis for parachute-vehicle system of Mars Pathfinder. *Chin. Space Sci. Technol.* **2018**, *38*, 63.
17. Shan, M.; Guo, J.; Gill, E. Deployment dynamics of tethered-web for space debris removal. *Acta Astronautica* **2017**, *132*, 293–302. [CrossRef]
18. Chang, Z.; He, J.; Hao, P.; Zheng, Z. Research on Human Falling Protection Performance Based on Safety Web. In Proceedings of the 2019 Prognostics and System Health Management Conference (PHM-Qingdao), Qingdao, China, 25–27 October 2019; pp. 1–8.
19. Xu, B.; Yang, Y.; Zhang, B.; Yan, Y.; Yi, Z. Bionic design and experimental study for the space flexible webs capture system. *IEEE Access* **2020**, *8*, 45411–45420. [CrossRef]
20. Zhen, M.; Yang, L.; Zhang, Q.-B. Ground collision test and simulation of space flynet. *J. Natl. Univ. Def. Technol.* **2018**, *40*, 171–176.